Investigating the Condensation of Benzene (C 6 H 6) in Titan's South Polar Cloud System with a Combination of Laboratory, Observational, and Modeling Tools

David Dubois, Laura T Iraci, Erika L Barth, Farid Salama, Sandrine Vinatier, Ella Sciamma-O'brien

▶ To cite this version:

David Dubois, Laura T Iraci, Erika L Barth, Farid Salama, Sandrine Vinatier, et al.. Investigating the Condensation of Benzene (C 6 H 6) in Titan's South Polar Cloud System with a Combination of Laboratory, Observational, and Modeling Tools. The Planetary Science Journal, 2021, 2 (4), pp.121. 10.3847/PSJ/ac06d5 . hal-03448629

HAL Id: hal-03448629
https://hal.science/hal-03448629

Submitted on 25 Nov 2021

The Planetary Science Journal, 2:121 (15pp), 2021 August https://doi.org/10.3847/PSJ/ac06d5

Investigating the Condensation of Benzene (C_6H_6) in Titan's South Polar Cloud System with a Combination of Laboratory, Observational, and Modeling Tools

David Dubois[1,2], Laura T. Iraci[1], Erika L. Barth[3], Farid Salama[1], Sandrine Vinatier[4], and Ella Sciamma-O'Brien[1]

[1] NASA Ames Research Center, CA, USA
[2] Bay Area Environmental Research Institute, CA, USA
[3] Southwest Research Institute, CO, USA
[4] LESIA, Observatoire de Paris, Université PSL, CNRS, Sorbonne Université, Université de Paris, France

Received 2020 December 25; revised 2021 March 19; accepted 2021 March 31; published 2021 July 1

Abstract

We have combined laboratory, modeling, and observational efforts to investigate the chemical and microphysical processes leading to the formation of the cloud system that formed at an unusually high altitude (>250 km) over Titan's south pole after the northern spring equinox. We present here a study focused on the formation of C_6H_6 ice clouds at 87°S. As the first step of our synergistic approach, we have measured, for the first time, the equilibrium vapor pressure of pure crystalline C_6H_6 at low temperatures (134–158 K) representative of Titan's atmosphere. Our laboratory data indicate that the experimental vapor pressure values are larger than those predicted by extrapolations found in the literature calculated from higher-temperature laboratory measurements. We have used our experimental results along with temperature profiles and C_6H_6 mixing ratios derived from observational data acquired by the Cassini Composite Infrared Spectrometer (CIRS) as input parameters in the coupled microphysics radiative transfer Community Aerosol and Radiation Model for Atmospheres (CARMA). CARMA simulations constrained by these input parameters were conducted to derive C_6H_6 ice particle size distribution, gas volume mixing ratios, gas relative humidity, and cloud altitudes. The impact of the vapor pressure on the CIRS data analysis and in the CARMA simulations was investigated and resulted in both cases in benzene condensation occurring at lower altitude in the stratosphere than previously thought. In addition, the stratospheric C_6H_6 gas abundances predicted with the new saturation relationship are ~1000× higher than previous calculations between 150–200 km, which results in larger particle sizes.

Unified Astronomy Thesaurus concepts: Titan (2186); Experimental techniques (2078); Laboratory astrophysics (2004)

1. Introduction

In Titan's dense atmosphere, complex hydrocarbon and nitrile species are produced from the dissociation of nitrogen (N_2) and methane (CH_4) and subsequent chemical reactions in the upper atmosphere, induced by solar UV radiation and electron bombardment from Saturn's magnetosphere. These gaseous species can become supersaturated and condense out as ices once they descend to the stratosphere (180–70 K, 1–100 mbar total pressure). The altitude where saturation occurs is a function of the mixing ratio of a particular species and atmospheric temperature. It is therefore likely to change with season and latitude, particularly in the fall at the pole where the decrease in stratospheric temperature is more dramatic and the mole fractions increase. A number of observations from Voyager, ground-based telescopes, and Cassini have pointed to the condensation of trace species in Titan's atmosphere. Many spectral signatures of hydrocarbon and nitrile ices have been observed at altitudes below 100 km (Coustenis et al. 1999; Khanna 2005a, 2005b; Samuelson et al. 1997; Kim et al. 2005; Anderson & Samuelson 2011; Anderson et al. 2014; Jennings et al. 2015). Recently, a cloud system was observed during the southern fall over the south pole at a much higher altitude (~300 km) and shown to contain HCN ice particles (Visible Infrared Mapping Spectrometer (VIMS) observations; De Kok et al. 2014; Le Mouélic et al. 2018) and benzene (C_6H_6) ice particles (Composite Infrared Spectrometer (CIRS) observations; Vinatier et al. 2018).

Closely after the northern spring equinox, which occurred in 2009, a change in the global atmospheric circulation, in agreement with general circulation model (GCM) predictions (e.g., Lebonnois et al. 2012; Lora et al. 2015; Newman et al. 2016; Vatant d'Ollone et al. 2020), was observed. The dynamical descending branch of a global circulation cell was observed at the south pole for the first time in 2010 June through an adiabatic heating that warmed up the mesosphere around 400 km and through enhancement of haze confined at latitudes higher than 80° S (Teanby et al. 2012; Vinatier et al. 2015). This descending branch also carried chemically enriched gas from the upper atmosphere, where molecules are formed, toward deeper levels. Molecular enhancements were observed for the first time in 2011 June above 400 km at the south pole, with the detection of increased mixing ratios for many species (e.g., C_2H_2, C_2H_4, C_2H_6, C_6H_6, HC_3N, and HCN; Coustenis et al. 2016; Mathé et al. 2020; Teanby et al. 2012; Vinatier et al. 2015). An unexpected thermal cooling was also observed at the south pole in 2012 January, at altitudes between 250 and 500 km (Teanby et al. 2017; Vinatier et al. 2015), that was mostly due to radiative cooling by the highly enriched molecules at high altitude, which overwhelmed the expected adiabatic heating due to the descending branch (Teanby et al. 2017). The decrease of solar flux during the southern fall also contributed to this thermal cooling. The simultaneous higher molecular mixing ratios combined with the strong cooling above the south pole (dropping temperatures below 120 K) created conditions where organic molecules could condense at unusually high altitudes (>250 km), leading to the appearance in 2012 of the high-altitude cloud system where C_6H_6 and HCN ice features were detected (De Kok et al. 2014; Vinatier et al. 2018).

By overlaying 100% humidity condensation curves on Titan's CIRS-derived temperature profile, it is possible to predict the approximate maximum condensation height of many of Titan's volatile inventory, knowing their vapor mole fractions (Anderson & Samuelson 2011; Barth 2017; Sagan & Thompson 1984) and thus demonstrate that C_6H_6 ice can condense at the altitudes observed by CIRS. Whether or not a cloud will form at a given altitude, however, depends on the availability of condensation nuclei and the ease with which nucleation of ice particles can occur. To address the nucleation process rigorously, microphysical models can be used to predict cloud vertical distribution for different molecular species present in Titan's atmosphere and expected to form clouds at different altitudes (see Methods section). These models use key input parameters from laboratory measurements (when available) and theoretical calculations, and constraints from observational data analysis (temperature profiles, atmospheric species abundances) to provide accurate predictions. Two important input parameters are the vapor pressure and condensation rate at relevant temperatures for the molecules of interest. Until now, C_6H_6 vapor pressures had been experimentally investigated only across the 184–350 K temperature range (e.g., Deitz 1933; Milazzo 1956; Jackowski 1974; Ha et al. 1976; De Kruif & Van Ginkel 1977; Lide 2006; Růžička et al. 2014). To investigate cloud formation in Titan's atmosphere, recent studies have used the Fray & Schmitt (2009) extrapolation of these experimental vapor pressures to lower temperatures (e.g., Vinatier et al. 2018, 2015; Rannou et al. 2019). These experimental data and their extrapolation to lower temperatures were insufficient, however, to allow microphysics models to successfully reproduce the formation of the observed benzene ice cloud system that formed in the south pole at 300 km altitude and aid in the interpretation of the observational data (e.g., Vinatier et al. 2018). Vertical temperature profiles as well as constraints on the gas-phase abundance of benzene on Titan, at the time and location the south pole cloud system was observed, are also critical data that are needed for a successful modeling of the cloud formation.

Here, we present the first results of a concerted experimental, modeling, and observational study addressing the chemical and microphysical processes leading to the formation of benzene ice cloud particles in the south polar cloud system, focusing on the CIRS observations at 87°S. Our synergistic approach relies on understanding and characterizing the physical behavior of C_6H_6 under temperature conditions relevant to Titan's cold (<180 K) atmospheric environment. We have measured, for the first time, the vapor pressures of benzene at Titan-like temperatures (134–158 K), for which no laboratory data were available. We have also reanalyzed CIRS data taken from 87°S to 68°S during the 2013 May 24 T91 flyby that provided temperature profiles and benzene mixing ratios needed as input parameters in the coupled Community Aerosol and Radiation Model for Atmospheres (CARMA) to explore the cloud variability. Our experimental data along with temperature profiles and C_6H_6 mixing ratios derived from CIRS observations were then used to constrain nucleation and condensation in CARMA, in order to determine expected cloud altitudes, gas volume mixing ratios (vmr's), and particle sizes.

2. Methods

2.1. Experimental Approach

2.1.1. Apparatus

The first step of our study employed the cloud nucleation and growth chamber developed as part of the NASA Ames Atmospheric Chemistry Laboratory (ACL) to measure the equilibrium vapor pressure of solid benzene for pressures and temperatures ranging from 1×10^{-7} to 1×10^{-4} Torr (1.3×10^{-3}–1.3×10^{-4} mbar) and temperatures from 134 K to 158 K, i.e., at Titan-relevant low temperatures (for a global overview of this project, the reader is referred to Dubois et al. 2019). The ACL apparatus is composed of a stainless-steel vacuum chamber (∼10 l volume; see Figure 1) continuously evacuated with a turbomolecular pump that provides a base pressure of $\sim 6 \times 10^{-8}$ Torr ($\sim 8 \times 10^{-8}$ mbar; Iraci et al. 2010). A 2.54 cm diameter, 2 mm thick silicon substrate is placed in the center of the chamber. As shown in the inset of Figure 1, a copper ring holds the silicon substrate and is connected to a vacuum-jacketed liquid nitrogen cryostat. A Kapton heater is mounted at the junction between the sample holder and the substrate, and a temperature controller allows the temperature of the mount and substrate to be adjusted. The temperature is measured with two *K*-type thermocouples on opposite sides of the copper mount as shown in Figure 1 (red dots). To prevent condensation on the vacuum-jacketed arm that connects the copper sample holder to the liquid nitrogen reservoir, a small amount of heating is applied via a second Kapton heater wrapped around the arm (gray hatch marks in Figure 1). Two glass bulbs, one containing liquid benzene and one containing cyclohexane (for the temperature calibration experiments described below), are connected to the chamber via stainless-steel delivery lines. The introduction of gas into the chamber is controlled by ultrafine all-metal leak valves (Lesker VZLVM940R), and the partial pressure of each gas is controlled by varying the flow into the chamber against the pumping; the resulting pressure is measured with a Terranova ion gauge calibrated to a Baratron capacitance manometer (0.1 Torr full scale, 0.13 mbar). KBr windows above and below the silicon substrate enable the passage of an infrared (IR) beam. The ice nucleation and growth on either or both sides of the silicon substrate are monitored by IR transmission spectroscopy to detect absorption bands of the deposited ice using a Nicolet Nexus 670 Fourier Transform Infrared (FTIR) spectrometer covering the 7000–500 cm^{-1} (1.4–20 μm) spectral range with a spectral resolution of 1 cm^{-1}. Figure 1 shows a schematic of the ACL experimental apparatus with the beam from the FTIR passing through the chamber KBr windows and the substrate before being detected by the DTGS detector of the FTIR. OMNIC software (series 8.3.103) is employed to calculate the integrated peak areas of the most intense bands. These integrated peak areas are used to detect ice onset, i.e., nucleation (indicated by a sharp increase), growth (a steady increase of intensity), and equilibrium (stable intensity).

2.1.2. Condensible Gas Preparation

Two separate glass bulbs were prepared, one with 5 ml liquid benzene (C_6H_6, HPLC grade, >99.9% purity—for the pressure gauge calibration and benzene equilibrium vapor pressure measurements), and the other with 5 ml liquid cyclohexane (C_6H_{12}, anhydrous 99.5% purity—for the temperature calibration). Once filled, the bulbs were placed, in turn, in a dry

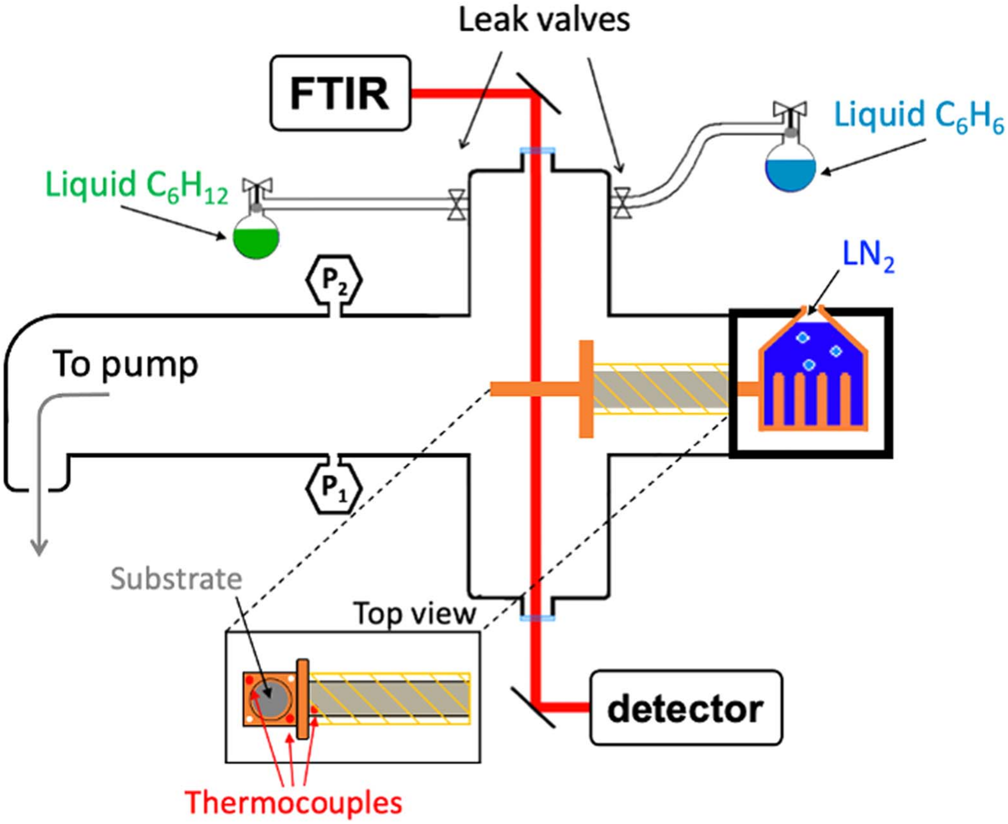

Figure 1. Schematic diagram (not to scale) of the experimental apparatus used for benzene ice condensation and growth studies (adapted from Iraci et al. 2010), including the capability for cyclohexane calibration measurements. Pressure is measured with a capacitance manometer (*P1*) and an ion gauge (*P2*). The inset shows a top view of the sample holder with the positions of the two *K*-type thermocouple gauges (red dots) used for temperature measurements, and a third one closer to the liquid nitrogen (LN2) dewar. The ice sample forms on either or both sides of the silicon substrate (gray), which is in the path of the IR beam. Infrared transmission spectra are collected with an external DTGS detector.

ice/ethanol slush (<−40°C) and freeze-pumped through a glass gas-handling manifold to remove any volatile impurities and residual air before being connected to the vacuum chamber via two separate stainless-steel delivery lines. The lines between the bulbs and the chamber were then pumped down, one at a time, through the vacuum chamber to purge them of any residual air (usually for 1–2 hr until a base pressure of $7–8 \times 10^{-8}$ Torr was reached, 9.3×10^{-8}–1.1×10^{-7} mbar). Once the base pressure was deemed satisfactory ($<1 \times 10^{-7}$ Torr, or 1.3×10^{-7} mbar) and stable conditions were reached, vapor was introduced from the bulb into the vacuum chamber (Figure 1). Note that the liquid samples were used for several experiments over several days. At the beginning of each day of experiments, the bulb to be used was frozen in a dry ice and ethanol slush, and any residual contaminants were pumped away through the vacuum chamber.

2.1.3. Pressure Measurement, Cross-calibration, and Uncertainty

An ion gauge can detect pressures several orders of magnitude lower than a capacitance manometer, but its readings are sensitive to the type of gas being measured. Thus, the ion gauge sensitivity factors for benzene and cyclohexane were determined by comparison to the gas-insensitive manometer in the region where their working ranges overlap. For benzene, three cross-calibration experiments were conducted over several days where benzene gas was admitted into the chamber while increasing the pressure from $\sim 10^{-5}$ to 10^{-4} Torr (1.3×10^{-5} to 1.3×10^{-4} mbar) in ∼10–12 increments. Each pressure condition was held constant for 3–5 minutes while the pressure was measured with both the ion gauge and the Baratron capacitance manometer. These time-invariant conditions were achieved in a flow regime (continuous inlet and pumping of gas). These calibration experiments provided an average C_6H_6 pressure correction factor of 6.24 for the ion gauge, by which the recorded "raw" ion gauge pressure was divided for the analysis of subsequent equilibrium measurement data. The same protocol was used for cyclohexane, with a resulting correction factor of 8.69 determined as the average of four independent cross-calibration experiments. The standard deviation among the replicate measurements for each gas was taken as the uncertainty in the respective ion gauge sensitivity factor: 2.2% for benzene and 12% for cyclohexane.

The overall uncertainty on pressures measured during benzene ice equilibrium experiments was determined through a square-root analysis of four contributing factors: (i) the uncertainty on the gas factor used to convert the ion gauge measurement to gas-independent measurements (i.e., 2.2% of the calibrated pressure), (ii) the uncertainty due to the assumption that 50% of the base pressure in the chamber corresponds to residual benzene vapor from a previous experiment (N.B.: this factor is generally negligible), (iii) the uncertainty due to the drift in pressure during the period of time the ice is kept at equilibrium (standard deviation of the pressure over the equilibrium time period), and (iv) the uncertainty due to the finite nature of the spacing between pressure steps, which can be assessed using the existing apparatus and protocol (generally the largest source of uncertainty).

Table 1
Experimental and Calculated Values Used to Determine Global Temperature Offsets for the Thermocouples

Date	P_{adj} (Torr)	T_{equ} (H76)	T_{equ} (J74)	T_{equ} Average (H76 + J74)	Observed T_{far} (K)	Observed T_{near} (K)	T_{far} Offset Average	T_{near} Offset Average
2/14/20	2.07E-05	147.85	149.27	148.56	157.48	156.36	−8.92	−7.80
2/17/20	1.15E-05	145.08	146.61	145.85	153.55	152.43	−7.70	−6.58
2/18/20	1.22E-05	145.35	146.88	146.11	155.09	153.91	−8.98	−7.80
3/5/20	2.66E-05	149.07	150.43	149.75	157.03	156.01	−7.28	−6.26
							−8.22	**−7.11**

Note. Observed T_{far} and T_{near} indicate temperatures measured at the two thermocouple locations.

2.1.4. Temperature Measurement, Calibration, and Uncertainty

As described earlier, in our experimental setup, the temperature is measured by two *K*-type thermocouples located on the substrate mount, on either side of the substrate. Calibration of the thermocouples was performed, prior to the benzene condensation experiments, by condensing cyclohexane (C_6H_{12}) vapors onto the silicon substrate. We chose to use cyclohexane because it is a compound with vapor pressures close to those expected of benzene at Titan-like temperatures (Jackowski 1974; Ha et al. 1976, hereafter referred to as J74 and H76, respectively), and because it has no reported phase transitions in the temperature range of interest, as opposed to water, which was historically used in our system to calibrate the temperature when running higher-temperature experiments. C_6H_{12} vapor was introduced into the chamber at pressures for which the ice onset temperature was expected to be between 134 K and 158 K. The temperature of the substrate was then reduced while monitoring the IR transmission spectrum to detect the nucleation of C_6H_{12} ice. IR-peak areas were integrated over the 2800–3000 cm^{-1} range corresponding to the $\nu_1 + \nu_2 + \nu_{12} + \nu_{13} + \nu_{17} + \nu_{18} + \nu_{25} + \nu_{26}$ asymmetric and symmetric C–H stretching modes of C_6H_{12} ice (NIST Standard Reference Database 35 and VPL Molecular Spectroscopy Database), in order to monitor the ice onset and growth. For each pressure condition, the temperature was lowered to 5–10 K above the expected saturation temperature (J74, H76) in coarse steps (2–3 K), then lowered further with finer 0.2–0.8 K increments until C_6H_{12} ice was detected. A sharp increase in the integrated peak area indicated ice onset (nucleation). The temperature was then reduced by several kelvin to allow for substantial ice growth, before being adjusted again to reach equilibrium (i.e., sticking and desorption compensating each other, resulting in the film mass, and thus the integrated peak area, remaining constant). This protocol was followed on most of the days when data were collected, and the raw equilibrium temperature measured with the thermocouples showed remarkable consistency (see Table 1 below). The thermocouple mounted closer to the liquid nitrogen and heater (called "near" as "near LN2" in Table 1; see Figure 1 for the location) always gave a result 1.0 ± 0.1 K colder than the thermocouple farther away ("far" in Table 1; see Figure 1). This may have resulted from differences in how well the sensors made contact with the mount, differences in their response due to manufacturing, or a true thermal gradient across the mount, and thus potentially across the silicon substrate.

For each C_6H_{12} temperature calibration experiment, the difference between each of the two recorded equilibrium temperature measurements and an average of the two available gas-vapor equilibrium parameterizations (H76 and J74) were calculated for each of the two thermocouple measurements. The resulting "near" and "far" temperature offsets were then averaged over all four calibration experiments to obtain an average offset term for each thermocouple (−8.2 K for "far" and −7.1 K for "near"; see Table 1). When analyzing experimental data, each thermocouple sensor was corrected with its respective offset term, and then the two calibrated thermocouple readings were averaged together as a best representation of the temperature at the center of the substrate where the IR transmission spectrum was acquired.

Overall temperature uncertainty was 1.3 K, as determined by the square root of the sum of the squares of the following contributing factors: (i) difference between literature values for cyclohexane equilibrium vapor pressure, (ii) reproducibility of the temperature calibration, (iii) uncertainty in the ion gauge sensitivity factor for cyclohexane, and (iv) finite nature of the spacing between temperatures measured during calibration. The first two terms dominated the overall uncertainty, in approximately equal proportions.

2.1.5. Benzene Equilibrium Experiments

For the C_6H_6 equilibrium experiments, the methodology differed slightly from the C_6H_{12} calibration measurements as the substrate temperature was kept constant and the benzene partial pressure was adjusted while monitoring the IR spectrum through the silicon substrate to detect the onset and growth of C_6H_6 ice. IR-peak areas were integrated for each of the four most intense bands corresponding to the ν_{11} C–H bending mode between 670 and 710 cm^{-1}, the ν_{18} twist mode between 960 and 1050 cm^{-1}, the ν_{19} C–C stretching modes between 1450 and 1500 cm^{-1}, and the $\nu_2 + \nu_{20}$ combined C–H stretching modes between 2950 and 3100 cm^{-1}. These bands, their assignments, and corresponding references are listed in Table 2. Note that we are following the Wilson notation (Wilson et al. 1955; Bernhardsson et al. 2000) for the band assignments. The ν_{11} band being the strongest absorption band for C_6H_6 ice in our spectral range, we focused on this particular integrated peak area to monitor the ice onset, growth, and equilibrium. Note that this ν_{11} band is the same spectral band that was observed with CIRS by Vinatier et al. (2018) and indicated as ν_4 using the Herzberg notation.

For each benzene equilibrium experiment, the substrate was first cooled to the temperature chosen for that specific experiment, then the IR spectra, pressure, and temperature acquisitions were initiated. A stable flow of benzene vapor was then admitted to the chamber at a pressure slightly below the

Table 2
Most Intense IR Bands Observed during Crystalline Benzene Ice Experiments Conducted below 146 K, Assignments and References

Wavelength (cm^{-1})	Assignment[a,b]	Mode	References
670–710	ν_{11} (ν_4)	C–H bend	[c, d]
960–1050	ν_{18} (ν_{14})	twist	[c, e, f, g, h]
1450–1500	ν_{19} (ν_{13})	C–C stretch	[c, e, f, g, h]
2950–3100	ν_{20} (ν_{12}) and others	C–H stretch	[c, f,g, h]

Notes. Band assignments follow the Wilson notation (Wilson et al. 1955). Notation according to the Herzberg convention are also given in parentheses (Herzberg 1966).

[a] Wilson et al. (1955).

[b] Herzberg (1966).

[c] Bernhardsson et al. (2000).

[d] Vinatier et al. (2018).

[e] Engdahl & Nelander (1985).

[f] Kearley et al. (2006).

[g] Dawes et al. (2018).

[h] Chandrasekaran et al. (2011).

expected nucleation point (J74; H76; Fray & Schmitt 2009, hereafter referred to as F&S09), then incrementally increased by 1%–15% until a sharp increase in the integrated peak area of the ν_{11} band was observed, indicating benzene ice onset (see Section 3.1.2); the closer to ice onset, the smaller the benzene flow increments (1%–5%). The pressure was kept constant for several minutes to allow the benzene ice layer to grow on the silicon substrate, then reduced by 1%–5% increments until the intensity of the integrated peak area of the ν_{11} band remained constant, indicating the ice film was no longer growing, thus in equilibrium with the vapor phase. The pressure measured during the time the ice was observed to be at equilibrium corresponded to the equilibrium vapor pressure for the experimental temperature recorded at that time.

2.2. Modeling: The Community Aerosol and Radiation Model for Atmospheres (CARMA)

The second part of our synergistic study used CARMA to simulate the nucleation and condensation (cloud altitudes, particle sizes, and gas relative humidity) of C_6H_6 at 87°S in Titan's atmosphere. CARMA simulates the microphysical evolution of aerosol particles in a column of atmosphere. In the study presented here, we used a recent version of the computational algorithms specifically designed for Titan applications (Barth 2017). In this Titan CARMA model, the particles are represented by a number of radius bins, defined by a user-specified minimum value and a mass ratio between bins. Both spherical and fractal aggregate particles can be modeled; for simplicity in this study, we used spherical particles. Titan's organic haze particles are represented by 35 radius bins beginning with a minimum radius of 1 nm and a mass ratio of 2. For C_6H_6 cloud particles, 28 radius bins are used with a minimum radius of 100 nm and a mass ratio of 2, which allows a maximum particle size of 50 μm. Each of these parameters can be varied. All particles are transported vertically through sedimentation and eddy diffusion, though eddy diffusion dominates for particles $\leqslant 0.1$ μm and it takes roughly 1 (terrestrial) year for a 1 μm particle to fall a distance of 10 km. All particles are also subject to coagulation. Collisions between involatile particle groups are generally handled by the equations for Brownian coagulation. The involatile haze particles in Titan's atmosphere accumulate charge, which decreases the sticking coefficient; this process is included in the Titan CARMA model following Borucki & Tripathi (1987) and Borucki et al. (2006). Coalescence kernels are calculated for cloud–cloud particle collisions. While coagulation is an important process in growing the haze particle population, we have generally found that not enough cloud particles are formed for efficient coalescence. Cloud particles are created through heterogeneous nucleation using the haze particles as cloud condensation nuclei. Here, nucleation follows the classical theory—calculated from the contact parameter between the C_6H_6 ice and aerosol nuclei. As the contact parameter approaches unity, the energy barrier goes to zero (Pruppacher & Klett 1997). Cloud particles then interact with the volatiles through condensational growth and evaporation. Cloud particle formation and growth are controlled by the surface tension and vapor pressure for the cold temperatures in Titan's stratosphere. For surface tension, we use the equation and constants found in Jasper (1972) and solve for ice–air interface equations following the method described in Curtis et al. (2005). For the benzene vapor pressures, the sublimation vapor pressure equation provided in F&S09 is generally used, but the experimental data used to construct that equation do not include temperatures below 184 K. In the study presented here, we used the experimental vapor pressures measured with the ACL facility as well as vapor pressure extrapolations by F&S09 and J74 to assess the impact of the vapor pressure values on the cloud altitudes, particle sizes, condensation curves, and gas relative humidity.

2.3. Observations: CIRS Analysis and Retrieval Methods

The third part of our interdisciplinary study was to reanalyze nadir CIRS observations of the south pole acquired with focal planes FP3 (600–1100 cm^{-1}) and FP4 (1100–1500 cm^{-1}) during the T91 Titan flyby on 2013 May 24 to determine the benzene gas mixing ratio close to its saturation level from 87°S to 68°S using the vapor pressure equation determined in this work. In Vinatier et al. (2018), a first analysis of this set of nadir observational data was performed to determine the horizontal distribution of the C_6H_6 ice cloud between 87°S and 68°S along with an analysis of T110 limb observations that allowed the determination of the C_6H_6 ice cloud vertical profile. In that study, the temperature profiles at each latitude were first derived by fitting the ν_4 CH_4 band at 1305 cm^{-1}, assuming a CH_4 vmr constant with altitude and latitude and equal to 1.48% (Niemann et al. 2010). The temperature profiles were subsequently used to generate synthetic spectra and retrieve molecular vmr's from the fits of molecular thermal emission rovibrational bands observed in the CIRS spectra. Once the contribution from the gas emission bands (C_2H_2 at 730 cm^{-1}, H_3CN at 663 cm^{-1}, CO_2 at 668 cm^{-1}, and C_6H_6 at 674 cm^{-1}) was removed, the remaining residuals still contained the ice spectral features, allowing for the detection of benzene ice at 682 cm^{-1} (Vinatier et al. 2018). In the study presented here, we used our experimental vapor pressures obtained at Titan-like temperatures to reanalyze the CIRS data from 87°S to 68°S and determine more accurate benzene gas mixing ratio profiles from the fits of the molecular gas emission band at 674 cm^{-1}. The temperature profile retrieved at 87°S by Vinatier et al. (2018) was also used as a constraint in the CARMA

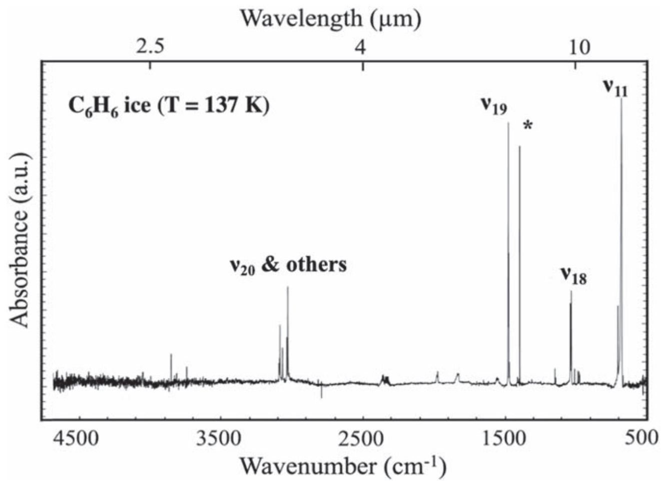

Figure 2. Infrared absorption spectrum of crystalline benzene ice acquired at 137.2 ± 1.3 K. The main bending and stretching modes are indicated. The most intense band (near 680 cm^{-1}) corresponds to the ν_{11} C–H bending mode (according to the Wilson notation), detected in the CIRS observations as reported by Vinatier et al. (2018). $*$ indicates an artifact feature due to the silicon substrate.

model. The cloud top level of C_6H_6 ice derived from the reanalysis of the CIRS observations was then compared to the predicted cloud vertical distribution obtained with CARMA to shed light on the cloud system vertical structure.

3. Results

3.1. Experimental Results

3.1.1. IR Absorption Spectra of Benzene Ice at Cold Temperature from 134 to 158 K

During each benzene condensation experiment, infrared absorption spectra were acquired every 40 s. At low temperature (<146 K) our measured spectra of crystalline benzene ice contained intense and narrow peaks. Figure 2 shows the spectrum obtained during an experiment conducted at 137.2 K ± 1.3 K. As listed in Table 2, the most intense bands correspond to the ν_{11} C–H bending mode near 680 cm^{-1} that was detected in the CIRS spectra by Vinatier et al. (2018), the ν_{18} twist mode around 1000 cm^{-1}, the ν_{19} C–C stretching mode around 1450 cm^{-1}, and the ν_2 and ν_{20} C–H stretching modes around 3000 cm^{-1}. Note that the band corresponding to the ν_{18} twist mode is the most intense band in a narrow spectral region around 1000 cm^{-1} that is populated with up to 12 vibrational modes due to three molecular vibrations: ring breathing, H wagging, and in-plane deformation (Kearley et al. 2006). Fundamental modes in the C–H bending region (2500–1500 cm^{-1}) are also visible but minor in intensity.

For the measurements conducted at higher temperatures (>146 K), however, the absorption bands appeared to either broaden (for the ν_{11} band), shift to longer wavelengths (for the ν_{19} band), or disappear (ν_{20} and others), compared to the spectra acquired at a lower temperature, as shown in Figure 3 (top, middle, and bottom panels, respectively). As discussed in more detail in Section 4.2, a possible explanation for the observed changes in spectral features could be a phase transition of the benzene ice from an ordered crystalline phase at lower temperatures (<146 K) to a partially disordered, but still crystalline, phase at warmer temperatures (>146 K).

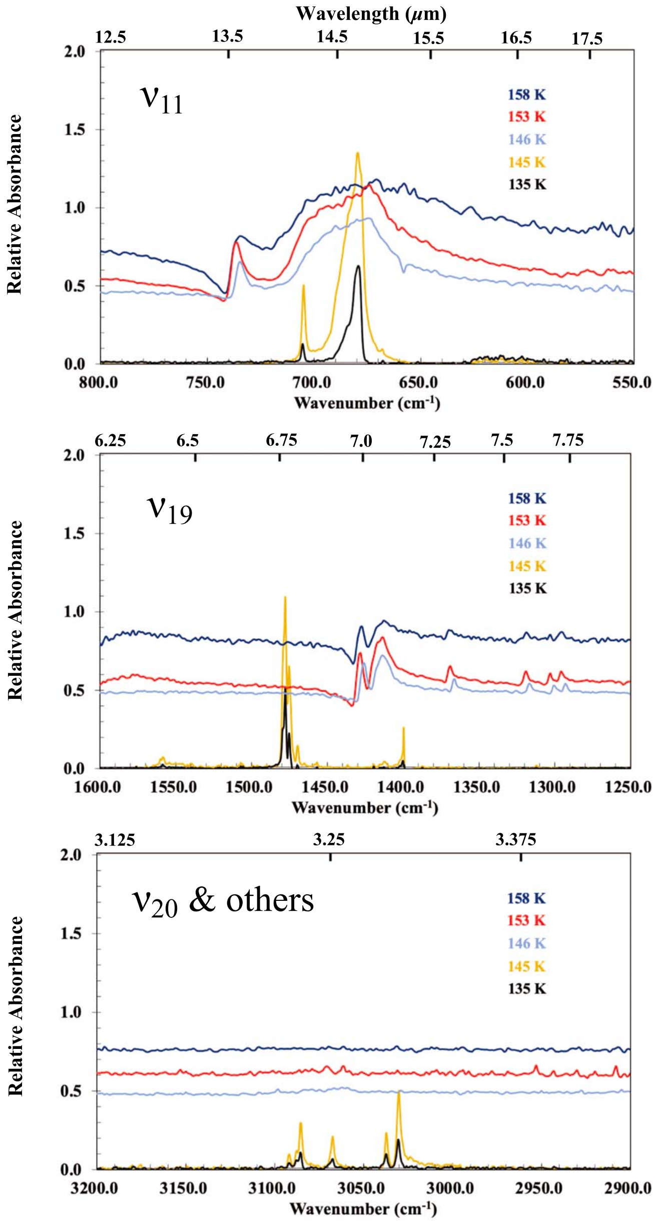

Figure 3. IR absorbance spectra of C_6H_6 ice films measured at five different temperatures, with a temperature uncertainty of ±1.3 K, all shown on the same relative intensity scale, with some spectra offset for clarity. Top: ν_{11} C–H bending modes around 680 cm^{-1}. Middle: ν_{19} C–C stretching modes around 1500–1450 cm^{-1}. Bottom: ν_{20} & others C–H stretch region around 3100–2950 cm^{-1}.

3.1.2. Benzene (C_6H_6) Equilibrium Pressure Determination

Benzene ice equilibrium experiments were conducted at 13 different temperatures between 134 K and 158 K, corresponding to equilibrium vapor pressures between 1×10^{-7} and 1×10^{-4} Torr (1.3×10^{-7}–1.3×10^{-4} mbar). As described in the Methods section, four IR-peak areas were integrated to monitor the four strongest bands in the spectral region covered by our spectrometer: 670–700 cm^{-1} (ν_{11}), 960–1050 cm^{-1} (ν_{18}), 1450–1500 cm^{-1} (ν_{19}), and 2950–3100 cm^{-1} ($\nu_2 + \nu_{20}$). The intensity of each peak area, integrated after baseline correction, was continuously acquired before, during, and after ice growth. As mentioned above, the ν_{11} band is the most intense band for the benzene ice in our spectral range, and thus it was preferentially used to monitor ice onset, growth, equilibrium, and sublimation, or the absence of ice.

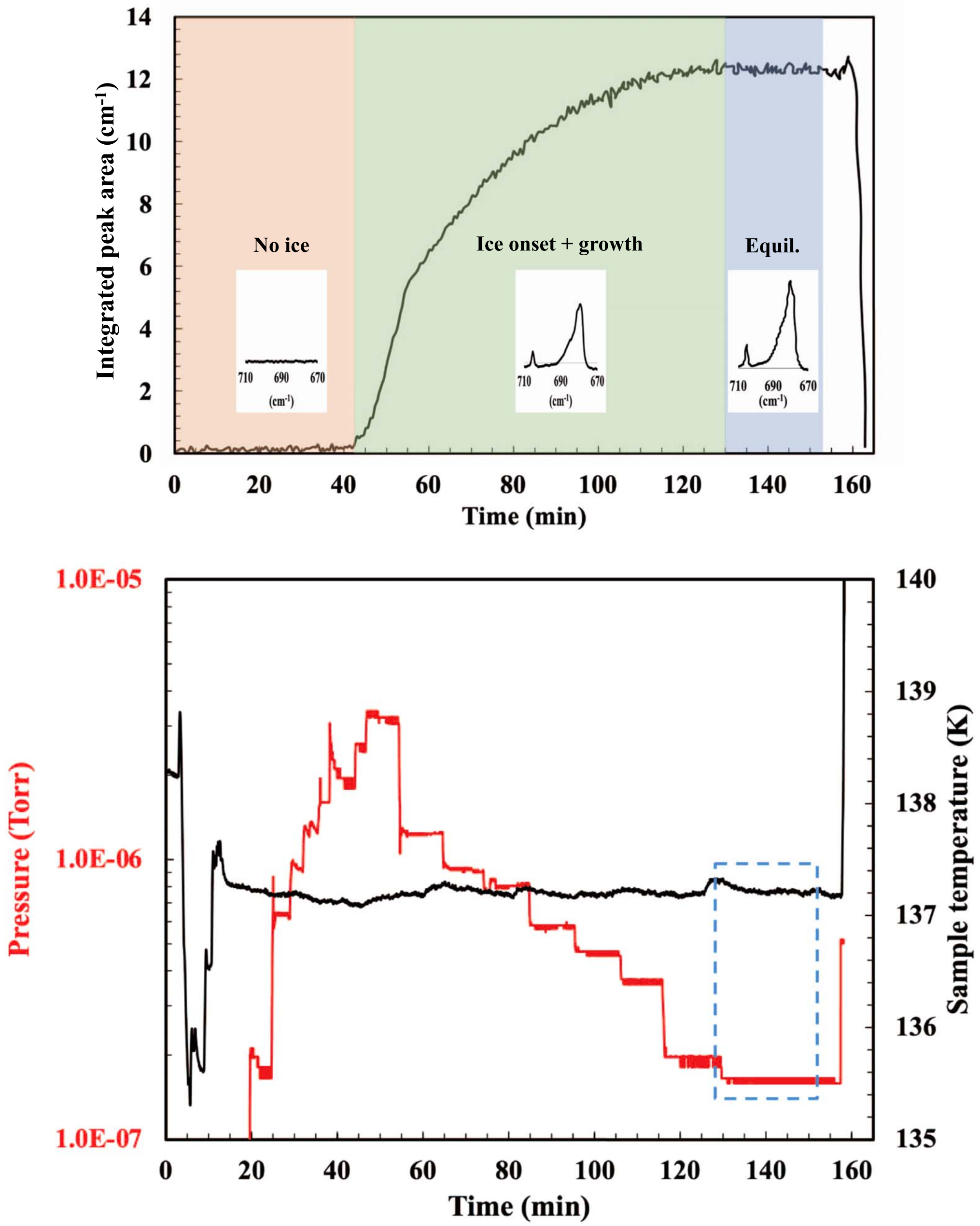

Figure 4. (Top) Integrated peak area of the ν_{11} C–H bending mode between 670 and 710 cm^{-1} during an experiment conducted with the substrate at $T = 137.2 \pm 1.3$ K, showing the ice onset and growth evolution (green shaded region) and the equilibrium (blue shaded region). At 160 minutes, the ice layer was rapidly sublimed by increasing the temperature of the substrate. Insets show spectra taken at ∼22 minutes (no ice), ∼62 minutes (ice begins to grow), and ∼147 minutes (equilibrium, time at which the spectrum from Figure 2 was collected) in the 710–670 cm^{-1} (14.1–14.9 μm) range. All spectra shown in the insets are on the same vertical scale. (Bottom) Calibrated experimental benzene vapor pressure (in red) and sample temperature (in black) measured during the same experiment. The dashed blue rectangle marks the equilibrium period.

The top panel of Figure 4 shows the ν_{11} integrated peak area acquired during an experiment conducted at 137.2 K ± 1.3 K. Shaded regions highlight the different stages of the experiment, from no ice (peach), to ice onset and growth (green), to equilibrium (blue). The experiment start time was at $t = 0$ minutes. Benzene ice started to form around $t = 40$ minutes (ice onset), as indicated by the rapid increase in the integrated peak area. The benzene ice was then allowed to grow for 10 minutes before slowly lowering the benzene vapor pressure by $\sim 5 \times 10^{-8}$ Torr steps (bottom panel), while keeping the sample temperature constant, until equilibrium was reached at $t = 130$ minutes. Equilibrium was maintained for 25 minutes. The sharp decrease in intensity after 160 minutes resulted from a rapid sublimation of the ice layer induced by dramatically increasing the temperature of the substrate in order to remove any benzene ice present.

Through post-analysis (see Sections 2.1.3 and 2.1.4), both the benzene ice sample temperature and vapor pressure measured during the equilibrium experiments were converted from "raw" to "calibrated" values. The bottom panel of Figure 4 shows a plot of the calibrated pressure and temperature during the equilibrium experiment showcased in the top panel. Before reaching the equilibrium vapor pressure, the temperature was kept constant while the pressure was lowered in incremental steps. In this experimental run, equilibrium was determined to be between 130

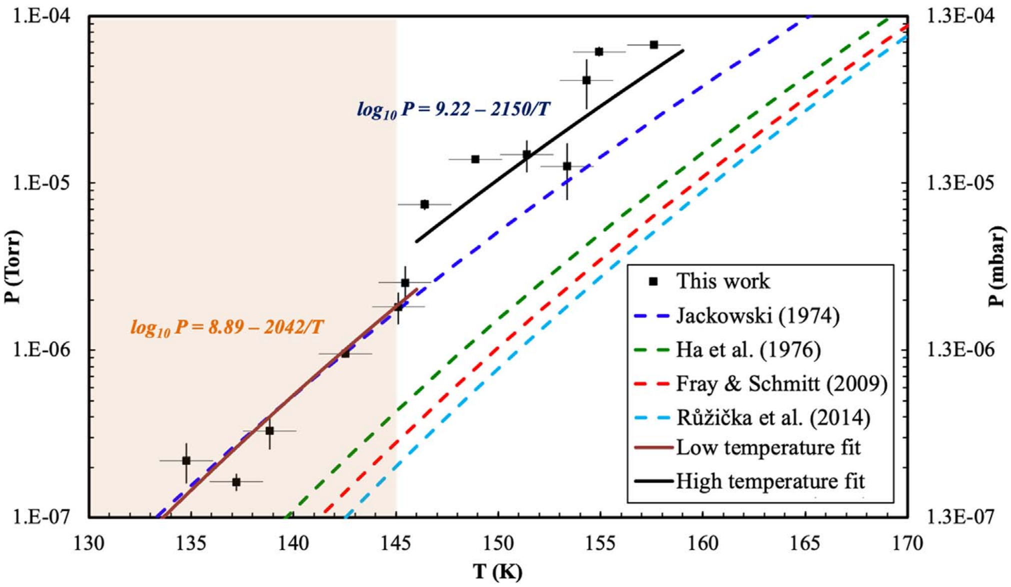

Figure 5. Experimental vapor pressure measurements of C_6H_6 ice (black) with associated temperature and pressure uncertainties, along with two new vapor pressure parameterizations fitted to the experimental measurements following the colder (134–146 K, brown) and warmer (146–158 K, black) temperature ranges. For comparison, the extrapolations (represented as dashed lines) from J74 (blue), H76 (green), F&S09 (red), and Růžička et al. (2014, cyan) parameterizations are also plotted on this figure. Pressures are given in both Torr (experimental measurement unit) and millibars (for comparison to observational data). The orange shaded area represents the temperature range relevant to Titan's stratosphere in the south pole in 2013 May, where benzene ice clouds were detected, i.e., <145 K.

and 155 minutes (blue dashed rectangle), when the corresponding averaged equilibrium temperature and pressure were 137.2±1.3 K and 1.6×10^{-7} Torr (2.1×10^{-7} mbar). Any temperature variations were found to be below our temperature calibration uncertainty.

3.1.3. Benzene (C_6H_6) Vapor Pressures at Titan-relevant Temperatures

The final vapor pressure measurements, including pressure and temperature error bars, are plotted in Figure 5 and provided in Table 3. The experimental data points measured are shown in black. Extrapolation curves (dashed lines) obtained from the parameterization of higher-temperature (solid lines) experimental vapor pressure measurements by J74, H76, F&S09, and Růžička et al. (2014) are also indicated in blue, green, red, and light blue, respectively.

For all experimental data points, we observe that, for a given temperature, the experimental vapor pressure is higher than the H76, F&S09, and Růžička et al. (2014) extrapolations, and for a given pressure, the associated temperature is 6–13 K colder. The experimental vapor pressures can be fitted with two slopes, one for temperatures <146 K that is almost aligned with the J74 extrapolation, and one for temperatures >146 K that is higher than the J74 extrapolation. This transition from one slope to another at 146 K corresponds to the transition observed in the IR spectra of the ice (see Figure 3). Only one experimental point warmer than 146 K is aligned with the J74 slope; however, this experimental data point has a large error bar (37%), as that data set was difficult to analyze, and the measured IR spectrum for that data point displays the same spectral features as those observed for all other higher-temperature data points. We have parameterized the two different slopes: one from the lower-temperature (<146 K) experimental data (Equation (1)) and one from the higher-temperature (>146 K) experimental data (Equation (2)) (where P is in millibars and T in kelvin):

$$\log_{10} P = 9.22–2150/T, \tag{1}$$

Table 3
Measured Benzene (C_6H_6) Equilibrium Conditions and Uncertainties (ΔT, ΔP)

T (K)	ΔT (K)	P (Torr)	ΔP (Torr)	P (mbar)	ΔP (mbar)
134.8	1.3	2.19E-7	5.97E-8	2.92E-7	7.96E-8
137.2	1.3	1.63E-7	1.95E-8	2.18E-7	2.60E-8
138.8	1.3	3.30E-7	7.41E-8	4.40E-7	9.88E-8
142.5	1.3	9.54E-7	5.13E-8	1.27E-6	6.84E-8
145.1	1.3	1.82E-6	3.88E-7	2.43E-6	5.17E-7
145.4	1.3	2.54E-6	6.60E-7	3.38E-6	8.80E-7
146.4	1.3	7.46E-6	5.30E-7	9.95E-6	7.07E-7
148.9	1.3	1.39E-5	3.94E-7	1.85E-5	5.25E-7
151.4	1.3	1.48E-5	3.23E-6	1.97E-5	4.31E-6
153.4	1.3	1.26E-5	4.68E-6	1.68E-5	6.24E-6
154.3	1.3	4.13E-5	1.36E-5	5.51E-5	1.81E-5
154.9	1.3	6.12E-5	4.04E-6	8.16E-5	5.39E-6
157.6	1.3	6.72E-5	3.58E-6	8.96E-5	4.77E-6

Note. Pressures are given in Torr (measured values) and millibars (for use in the interpretation of observational data).

$$\log_{10} P = 8.89–2042/T. \tag{2}$$

Because the temperature regime in Titan's atmosphere at the south pole where the benzene ice cloud was observed is less than 146 K, it was more appropriate for our study to use the low-temperature experimental parameterization (Equation (1)) to derive the benzene mixing ratio from the CIRS data and to conduct modeling of the cloud formation with CARMA. To determine the impact of the new experimental vapor pressure on the model, we have also used the J74 and F&S09 extrapolations with CARMA.

3.2. Reanalysis of CIRS Nadir Data: Spatial Distribution of the C_6H_6 Polar Cloud of 2013 May

In order to investigate the impact of the new vapor pressure measurements on the altitude of the cloud top derived from the Cassini/CIRS observations, we have reanalyzed the nadir CIRS observational data from 2013 May previously studied by Vinatier et al. (2018, see their Figure 2) and covering the 68°S to 87°S latitudes. The thermal profiles were derived from the CIRS data in Vinatier et al. (2018, see their Figure 3(a)). We retrieved the C_6H_6 gas vmr profile and the pressure level at which C_6H_6 is expected to condense, at each latitude, using the experimental vapor pressure parameterization obtained by fitting the cold temperature (<146 K) measurements (Equation (1)). In our atmospheric model, we assume that the C_6H_6 vmr cannot be larger than its saturated value so that when the vmr profile reaches saturation, it becomes equal to the saturated value. Figure 6 shows the new vmr profiles of C_6H_6 gas derived using our experimental C_6H_6 vapor pressure parameterization (Equation (1)) for the 134–146 K temperature range (in red), compared to the vmr profiles inferred by Vinatier et al. (2018) using the F&S09 extrapolation (in black).

Using our experimental C_6H_6 vapor pressure measurements, which are larger than those derived from the extrapolation of F&S09, results in a condensation of C_6H_6 occurring deeper in the stratosphere. With a higher vapor pressure, saturation occurs at lower altitudes. For the CIRS data at 87°S, 83°S, and 68°S, our new analysis using the experimental vapor pressure parameterization results in C_6H_6 saturation occurring about 30 km deeper than inferred in the study conducted by Vinatier et al. (2018) that considered the F&S09 vapor pressure extrapolation. For the CIRS data at 73°S, the C_6H_6 condensation would occur 50 km deeper. The most dramatic change is seen for 78°S, where C_6H_6 condensation would occur about 130 km deeper compared to retrievals obtained with the F&S09 extrapolation. With this new analysis of the CIRS observational data, we derive a cloud top that would be located between 256 and 246 km in the 87°S–83°S region and would be observed around 90 km in the 78°S–68°S latitude region.

3.3. Modeling: Stratospheric C_6H_6 Ice Cloud Particle Formation and Particle Size Distribution

We have simulated the formation of benzene clouds in the southern polar atmosphere with the CARMA model. In the model, the atmospheric column extends from 30 km to 400 km with 1 km grid spacing. This allows us to cover the altitude region probed by CIRS (80–550 km) while also simulating the evolution of the cloud particles at lower altitudes through the tropopause around 40 km, a level that is too deep to be probed by CIRS. For our study of the south polar cloud, we initialized the model with the temperature/pressure profile from CIRS data at 87°S retrieved by Vinatier et al. (2018) (see Figure 3(a)). The descending branch of Titan's circulation cell observed after the northern spring equinox was included in the model by calculating a downward vertical wind with a magnitude of 2.5 mm s^{-1} at 380 km, as indicated by the CIRS data, and scaled with the atmospheric density profile through the base of the model domain. Benzene vapor is included as a tracer in the model. It is constantly supplied by an inward flux across the model top boundary and can be lost through diffusion across the model bottom boundary. For this study, we initialized the model with a vmr of 1.8×10^{-6} to match the value inferred from our reanalysis of the CIRS 87°S observation at 300 km (∼0.017 mbar). The flux across the top of the atmospheric column (4×10^{12} m^{-2} s^{-1}) was calculated to maintain the observed mixing ratio at 300 km.

The model includes a distribution of haze particles that serve as condensation nuclei, along with their steady-state profile and flux. These were generated in a previous simulation done without the cloud microphysics. Benzene cloud particles form through nucleation once a layer of atmosphere reaches saturation with respect to benzene vapor. The nucleation equation (see Barth & Toon 2003) includes a number of parameters that had not been widely studied for the case of benzene in Titan's atmosphere before this work. The most significant of these parameters are the surface energy, vapor pressure, and critical saturation (S_{crit}) for nucleation onset. We followed the method described in Curtis et al. (2005) to calculate the surface energy from the heat of fusion. We simulated benzene cloud formation using our cold temperature experimental benzene vapor pressure parameterization (Equation (1)) as well as the F&S09 and J74 vapor pressure extrapolations to compare the modeling outputs (C_6H_6 ice particle size distribution, gas vmr's, gas relative humidity, and cloud altitudes) and assess the impact of the vapor pressure on the results. The vapor pressure controls the cloud particles' formation, but also the rate at which they grow, by condensing additional vapor, or evaporate, if the environment becomes subsaturated.

We have calculated the condensation curves of C_6H_6, using the J74 and F&S09 extrapolations and our cold experimental data parameterizations, for both the temperature and pressure conditions at the south pole in 2013 and at the Huygens landing site in 2005. They are plotted on the left panel of Figure 7 against the temperature profile inferred from the analysis of CIRS observational data at 87°S (Vinatier et al. 2018) and the temperature profile measured by the Huygens Atmospheric Structure Instrument (HASI; Fulchignoni et al. 2005). A dramatic decrease in stratospheric temperatures is clearly observed at the pole where temperatures as low as 100 K were observed, compared to the 186 K temperature measured at the equatorial stratopause (250 km) by HASI. Where the condensation curves intersect with the temperature profile indicates where C_6H_6 saturation is expected to occur. All condensation curves associated with the CIRS 87°S temperature profile indicate a C_6H_6 saturation level at the south pole between 260 and 280 km, whereas the condensation curves associated with the HASI temperature profile at the equator in 2005 indicate a C_6H_6 saturation level below 100 km. As noted previously, the temperature conditions observed at the south pole after the northern spring equinox enabled the condensation of volatiles at much higher altitudes than in nonwinter, nonpolar conditions. The larger molar fractions and substantial decrease in stratospheric temperatures near-polar latitudes resulted in supersaturation occurring at higher altitudes, as shown by the saturation curves. The saturation altitudes predicted for the temperature and mixing ratio observed at 87°S are about 3× higher than those predicted for the temperature and mixing ratio profiles observed by the Huygens instruments at the equator in 2005.

The right panel of Figure 7 shows the C_6H_6 gas vmr calculated with CARMA using the F&S09 and J74 vapor

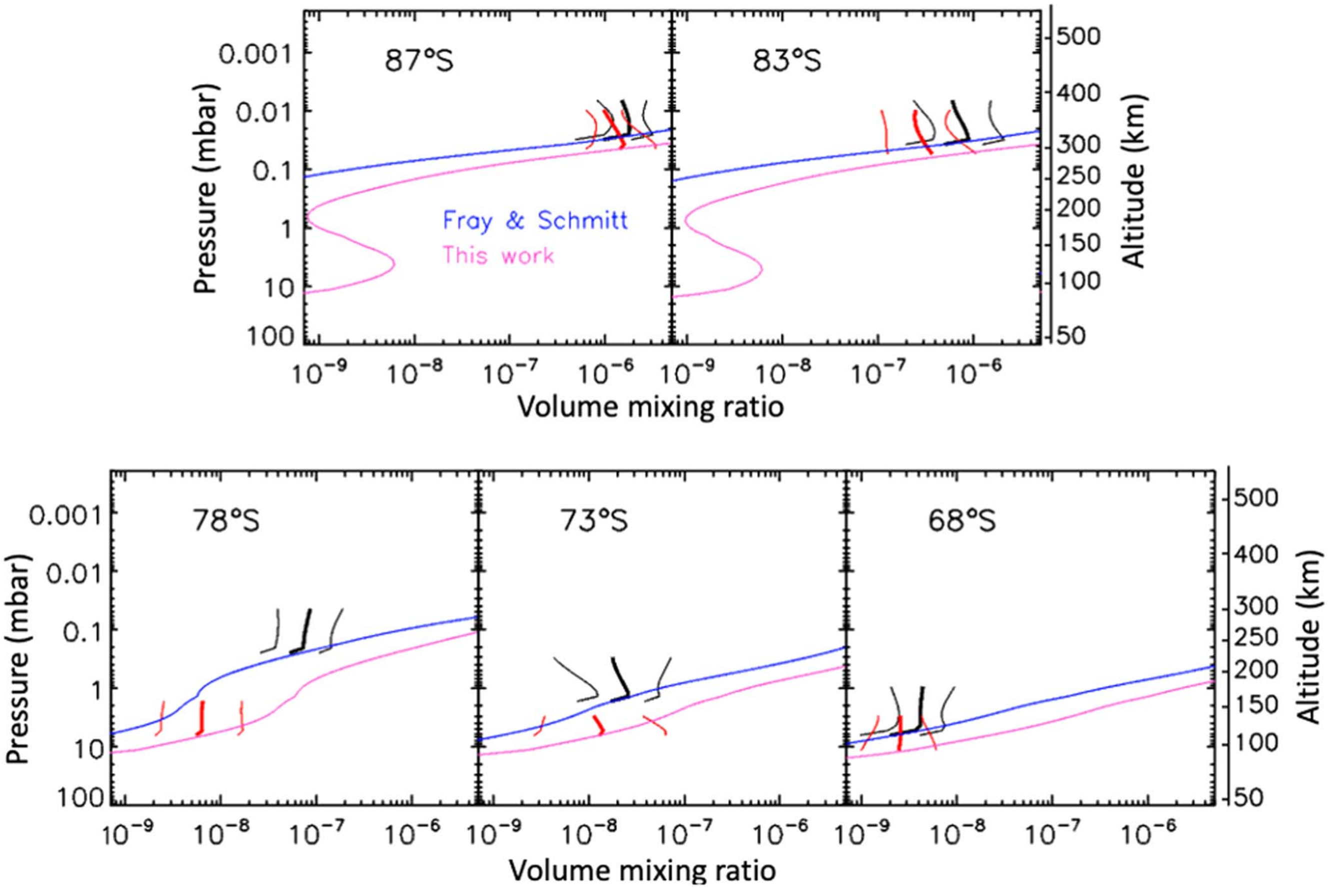

Figure 6. Volume mixing ratio profiles of C_6H_6 inferred from CIRS data acquired at 87°S, 83°S, 78°S, 73°S, and 68°S by Vinatier et al. (2018, black) using the F&S09 C_6H_6 vapor pressure parameterization (blue) compared to profiles obtained in this study (red) from the reanalysis of CIRS data using our cold temperature (134–146 K) experimental C_6H_6 vapor pressure parameterization (pink). Thick and thin lines (for both black and red) represent the inferred profiles and associated errors, respectively.

pressure extrapolations as well as our experimental colder temperature (<146 K) parameterization (Equation (1)). We observe that, at the top of the stratosphere, where benzene remains subsaturated (>250 km), the C_6H_6 gas vmr profile is unaffected by the cloud microphysics processes occurring at lower altitudes and therefore remains independent of the vapor pressure parameterization. At lower altitudes, however (∼250 km to near the tropopause), which correspond to lower temperatures ($T < 130$ K), the C_6H_6 vmr profile is strongly affected by cloud microphysics as we observe that the C_6H_6 vmr calculated with the J74 extrapolation or our experimental parameterization (i.e., with higher vapor pressures than F&S09) is about three orders of magnitude higher than the C_6H_6 vmr obtained with the F&S09 extrapolation. We conclude that below 250 km the C_6H_6 vmr profile is controlled by cloud microphysics. In the troposphere near 50 km, all calculated C_6H_6 vmr profiles reach minima below 10^{-20}. At these tropospheric altitudes, the C_6H_6 gas vmr becomes negligible and is at least nine orders of magnitude lower than at stratospheric levels. This can be explained by supersaturation followed by the condensation of C_6H_6 in the stratosphere, which effectively depletes it from the gas phase as the temperature profile decreases overall at lower altitudes.

In order to reach steady state, the microphysics model simulations were run for a total of 200 terrestrial years (∼6.75 Titan years). Vertical profiles of the benzene cloud particle physical parameters and the effect of changing the vapor pressure parameterization used to model them are shown in Figures 8 (number density, relative humidity) and 9 (size distribution). The impact of the vapor pressure on the density of particles (Figure 8, left panel) is mostly visible in the lower stratosphere, where using a more volatile vapor pressure equation like the J74 extrapolation (blue) or our experimental parameterization (orange), compared to the F&S09 extrapolation (red), results in almost two orders of magnitude fewer particles below 150 km. At higher altitudes (>200 km), where condensed benzene is observed, the effect is noticeably smaller. This highly altitude-dependent layering effect can also be seen in the simulated benzene gas relative humidity with respect to ice (Figure 8, right panel). In supersaturation conditions (>100%, above 200 km), using the J74 extrapolation or our experimental data parameterization results in a cloud top found ∼10 km below that calculated with the F&S09 extrapolation. This strong layering geometry of C_6H_6 particles (detailed previously in Barth 2017) approximately follows the overall condensation altitude in Figure 7, although with a decrease of ∼20 km with the J74 extrapolation and our experimental data parameterization (Figure 8, right panel). The decrease in altitude between where the calculated condensation curves intersect with the temperature profile (Figure 7, left panel) and where the cloud tops are predicted to occur is primarily due to the fact that we initialized these simulations to calculate a nucleation rate of $1\ \mathrm{cm}^{-2}\ \mathrm{s}^{-1}$ at a critical saturation of $S_{\mathrm{crit}} = 1.35$ and temperature $T_{\mathrm{crit}} = 125$ K. These values of S_{crit} and T_{crit} are not for benzene, as those have not been measured yet. However, they were estimated,

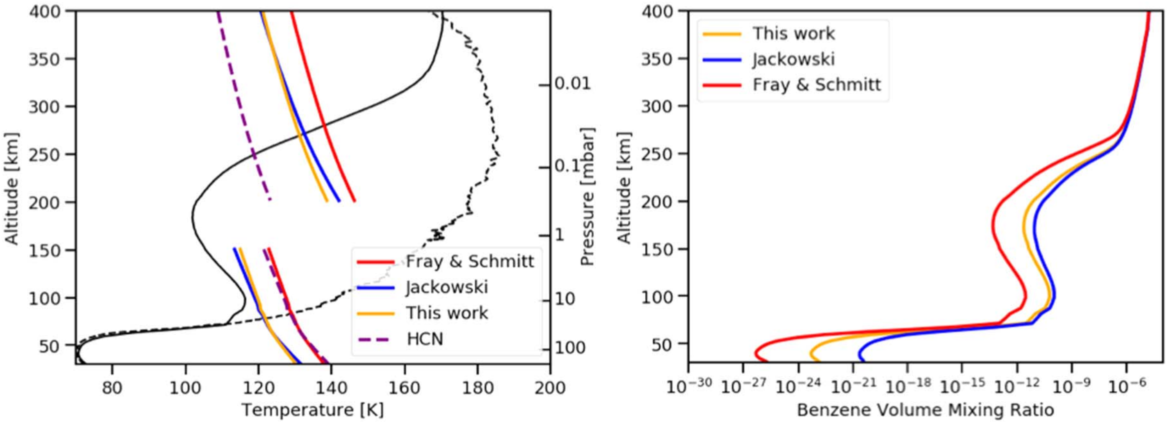

Figure 7. Left: vertical temperature profiles retrieved from nadir CIRS observations (Vinatier et al. 2018) near the south pole at 87°S after the northern spring equinox (black, solid) and measured by the HASI (black, dashed) at the equatorial Huygens landing site in 2005 (Fulchignoni et al. 2005). Condensation curves of C_6H_6 calculated with our new colder temperature vapor pressure (orange) parameterizations as well as the J74 (blue) and F&S09 (red) extrapolations are plotted against the temperature profiles. The top set of condensation curves were calculated with the vmr derived from our reanalysis of the CIRS data at 87°S, and the bottom set with the vmr at the equator from Barth (2017). The HCN condensation curves for these two conditions are also shown for comparison (purple, dashed). Right: benzene gas vmr calculated using our experimental cold (<146 K) vapor pressure parameterization (Equation (1), orange) and the vapor pressure extrapolations from F&S09 (red) and J74 (blue).

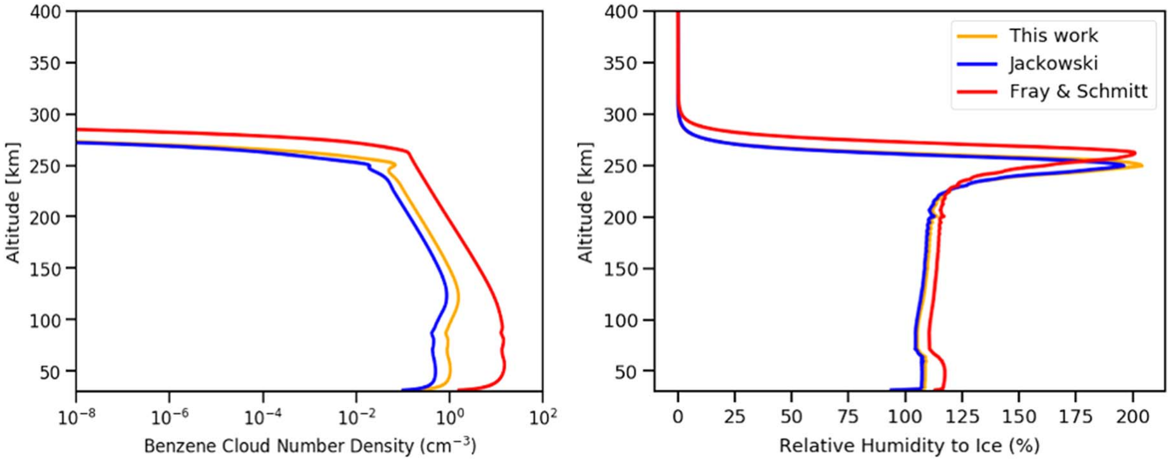

Figure 8. Left: number density profile for C_6H_6 clouds. Using the J74 extrapolation (blue) or our experimental parameterization (orange) (i.e., higher vapor pressures than F&S09, red) results in a smaller density of particles. Right: vertical profile of the C_6H_6 gas humidity relative to ice using the same three parameterizations.

guided by nucleation experiments conducted on other hydrocarbon materials present in Titan's atmosphere (Curtis et al. 2005, 2008). Nucleation experiments with benzene will be conducted in the future, but in the meantime in the present work, we performed sensitivity tests on the nucleation rates by considering an easier case ($S_{crit} = 1.1$) and a harder case ($S_{crit} = 1.5$) as described in Barth (2017). The cloud particles in the $S_{crit} = 1.5$ case are nearly identical to those in the $S_{crit} = 1.35$ case. For the easier nucleation case ($S_{crit} = 1.1$), the number of cloud particles increases by a factor of ~3; this is uniform with altitude above about 100 km and then the curves begin to converge.

The sensitivity of particle size distribution to the vapor pressure equations used can be seen in Figure 9. The C_6H_6 particle size distribution at stratospheric and tropospheric altitudes was calculated using the F&S09 and J74 vapor pressure extrapolations as well as our cold temperature (<146 K) experimental parameterization. Using the F&S09 (Figure 9(a)) vapor pressure extrapolation results in a size distribution overall uniform with altitude, with a slight increase in size from ~0.3 μm to ~0.5 μm from 250 km down to 50 km, respectively. Using the J74 vapor pressure extrapolation (Figure 9(b)), and similarly the new experimentally derived parameterization (Figure 9(c)), results in a wider size distribution, with peak radii varying from ~0.2 μm to ~1 μm in the same altitude range. The scaled particle densities are slightly smaller in the latter case than in the former. The size distribution curves for all three cases shift to larger radii as the cloud particles descend through the atmosphere. Because growth by condensation is proportional to the vapor pressure, in the cases where the J74 and experimental vapor pressures were used, the particles grow at approximately the same rate, whereas in the case where the F&S09 vapor pressures were used, growth proceeds at a rate ~30× slower. Also, for the case using the F&S09 extrapolation, the growth timescales are typically longer than the fall timescales and so the particles overall remain smaller than for the other two cases.

The curves for J74 and this work are less uniform than for F&S09. At 250 km, where the peak in cloud formation is occurring, the growth rates are also substantially higher than at other altitudes, and this is evident in the double-peaked structure of the curve, showing a nucleation mode at smaller radii and a

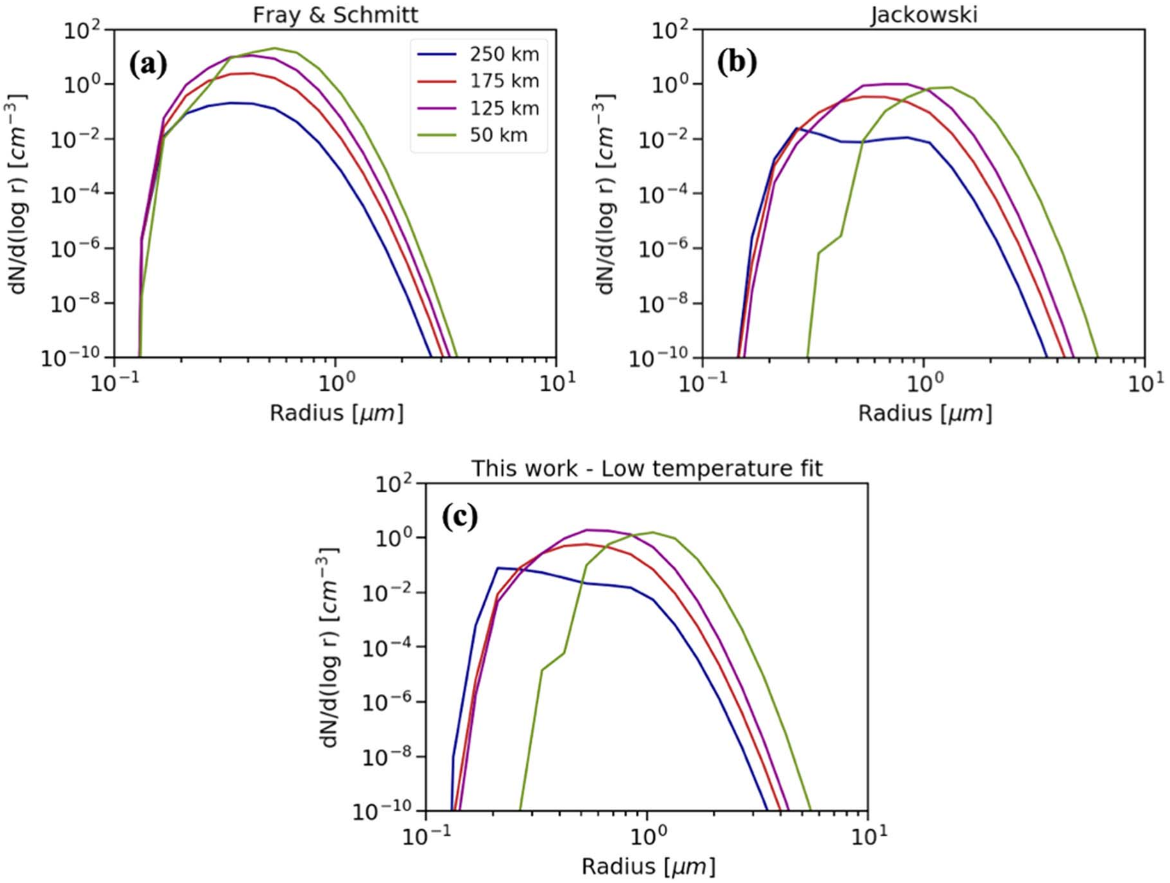

Figure 9. Benzene ice particle radius distribution at four different altitudes, from 250 km down to 50 km (see legend for color code), calculated using (a) the F&S09 vapor pressure extrapolation, (b) the J74 extrapolation, and (c) the new cold temperature (<146 K) experimental vapor pressure parameterization, which is similar to J74. With a higher vapor pressure (this work), the peak particle size increases at all altitudes.

growth mode at larger ones. A double-peaked structure begins to appear again below 100 km and is seen here in the 50 km curves. Figure 8 (right panel) shows the relative humidity here to be 105%–110%, which is much too low for nucleation to be occurring. Instead, the emerging peak at small radii is the result of evaporation of particles at the small end of the size distribution due to the Kelvin effect, which is due to the pressure difference between the ice particle and the surrounding air.

Previous simulated size distributions were roughly divided into three major groups for various volatiles found in Titan's atmosphere (Barth 2017), with C_6H_6 forming the smallest particles with peak radii of ∼1 μm. This coincides with what is calculated here at the lowest altitude (50 km). However, mainly due to a much more substantial condensational growth of C_6H_6 in polar conditions, the size distributions of C_6H_6 particles seen here at higher altitudes are only comparable with those found by Barth (2017) at lower altitudes. The predicted particle size distribution is consistent with the 1.5 μm upper limit derived by Vinatier et al. (2018) from the fit of the ν_{11} C_6H_6 ice band observed by CIRS.

4. Discussion

4.1. Impact of the Higher Vapor Pressure of Pure Benzene Ice on Stratospheric Condensation

This study has enabled us to assess the impact of the vapor pressure values on a number of processes related to benzene cloud condensation. In particular, using the vapor pressure in CARMA simulations allows the computation of the C_6H_6 gas mixing ratio as a function of altitude below ∼300 km, which cannot be done from CIRS data (as the C_6H_6 vmr of the vapor is assumed in the model to be following its condensation curve). We have observed that using the F&S09 and J74 vapor pressure extrapolations and our cold temperature experimental vapor pressure parameterization (Equation (1)) results in stratospheric C_6H_6 vapor abundances that significantly differ (∼1000×) between ∼100 km and ∼250 km depending on which parameterization is used. This directly impacts the cloud number density profile (Figure 8) and therefore the particle size distribution (Figure 9). When using our experimental vapor pressure parameterization, we predict a clear growth in particle size from the remaining C_6H_6 gas below the condensation level, due to significantly more benzene gas being available per cloud particle for condensation to begin with. This is also the case when using the J74 extrapolation. This could have implications for potential condensation and co-condensation processes with other organic ices as discussed below.

With the global circulation reversal following the northern spring equinox, air masses enriched in photochemically produced volatiles descended into regions with temperatures favorable for their condensation. Most recently, the effect of changing the vapor pressure equations on the calculated volume gas mixing ratio, number density, and size distribution of organic particles was investigated in Barth (2017) for several organic vapors in Titan's atmosphere. Using our new experimental vapor pressure parameterization in CARMA simulations has revealed unexpected effects on the nucleation and growth of C_6H_6 ice particles in the stratosphere, including a larger C_6H_6 gas vmr at stratospheric altitudes (Figure 7) below the condensation level, compared to those calculated from the F&S09 extrapolation, which has been used in the past for the interpretation of Titan observational data. This observed impact of using different vapor pressure equations on the gas vmr is in agreement with the results of Barth's (2017) study, even though the latter was conducted using a very different temperature profile.

When using a higher C_6H_6 vapor pressure in the calculations (as determined in this study), we observe a larger spread in the size distribution of benzene ice particles simulated in the polar cloud system at 87°S (Figure 9). The size distribution remains relatively homogeneous between ~250 km and ~175 km, but reaches a peak radius of ~1 μm deeper in the atmosphere (<100 km). In these conditions, the higher vapor pressure results in growth rates that are faster than the particle fall speeds, and so particle growth can attain larger peak radii. The number of particles simulated here with radii ~0.6–1 μm is larger than what was calculated from the Huygens landing site temperature profile (which used the F&S09 extrapolation) by over an order of magnitude. These experimental insights thus indicate that with a higher C_6H_6 vapor pressure, ice particles can grow larger in size from the stratosphere deeper down in the troposphere.

Low altitudes at the polar region are also speculated to harbor co-condensed ices in conditions where lower temperatures favor gas-to-solid transitions. In particular, putative co-condensed ices have been shown to match CIRS observations (Anderson et al. 2018), and species such as C_6H_6 and HCN, two important photochemically produced molecules in the atmosphere, appear to be crucial in the interpretation of CIRS spectra. Barth (2017), using the F&S09 extrapolation to calculate the benzene condensation curve, showed that C_6H_6 and HCN were predicted to condense at near-identical altitudes for the temperature profile observed at the Huygens landing site (see Figure 7, left panel). With the temperature profile at 87°S, however (and newly derived polar abundances from the CIRS data), using the F&S09 C_6H_6 vapor pressure extrapolation results in condensation curves of HCN and C_6H_6 that do not overlap. Furthermore, for the temperature profiles at both 87°S and the Huygens landing site, using our experimental vapor pressure parameterization also results in condensation curves of HCN and C_6H_6 that do not overlap. From the results of the study presented here, it appears that C_6H_6 polar cloud particles form first (at higher altitudes) and continue to exist at all altitudes down to the tropopause. At slightly lower altitudes, HCN saturates and co-condensation becomes possible beginning at ~250 km, which is also the altitude of the peak in the benzene nucleation rate when using our experimental vapor pressure parameterization. Thus, in spite of the ~10 km difference in the saturation levels between C_6H_6 and HCN, co-condensation between these two molecules is still possible at altitudes below the HCN saturation level. At these polar latitudes, the results obtained here are therefore not contrary to the idea of co-condensation of C_6H_6 and HCN in the stratosphere (e.g., Gudipati et al. 2013; Anderson et al. 2016).

4.2. Crystallinity and Phases of C_6H_6 Ice in the Laboratory and in Titan's Stratosphere

The geometry and molecular orientation of some organic and nonorganic ices are known to change according to temperature (e.g., Grundy et al. 1993, 2002; Quirico 1995). For astrophysically relevant ices (Titan, Pluto, Triton, comets), retrieving optical properties in the laboratory is an important step to supplement existing spectral retrievals of planetary surfaces. On atmosphere-less icy moons, as well as in Titan's atmosphere, measuring temperature-dependent spectra of thin ice films is crucial in order to obtain relevant absorption coefficients of these ices. Both intense and weaker bands need to be measured to assess, for example, the compositional fraction of organics (diluted versus pure) from remote-sensing techniques (e.g., see the methane study by Grundy et al. 2002). The temperature dependence of ice spectral features (both in band intensity and band broadening) can be attributed to phase transitions due to local disorder (orientational or rotational) and molecular geometry. This effect has been studied for CH_4 ices in N_2 matrices (Nelander 1985), CH_4 ice I (Grundy et al. 2002), N_2 ice (Grundy et al. 1993), and SO_2 (Quirico et al. 1996). By combining experimental and theoretical calculations, Nelander (1985) showed that methane could rotate when trapped in solid N_2, provided that substitutional sites had an identical symmetry as methane trapping sites. These transitions result in a reversible broadening of IR absorption bands. The temperature-dependent broadening and coalescing of CH_4 ice features reported by Grundy et al. (2002) clearly show this phenomenon. The crystallographic phase transition and band broadening for CH_4 are notable near 1270 cm^{-1} when increasing temperature from 20 K to 93 K (Figure 2 in Grundy et al. 2002).

In our experimental study, we conducted benzene ice experiments from 134 to 158 K and observed changes in the absorption spectra from the lower-temperature regime (134.8–145.4 K) to the higher-temperature regime (146.4–157.6 K) as shown in Figure 3. The observed shifting, broadening, and coalescing of the benzene ice absorption bands are consistent with the transitions from an ordered crystalline phase at lower temperatures to a partially disordered, but still crystalline, phase at warmer temperatures reported by Grundy et al. (2002) for CH_4. To our knowledge, no dedicated crystallographic and spectroscopic studies of these temperature-sensitive phenomena have been conducted for C_6H_6 ices, but they would be of great interest (similar to, e.g., Dawes et al. 2017 although those were performed at colder temperatures), as they would expand our understanding of low-temperature C_6H_6 ice properties. We note that in a recent study by Mouzay et al. (2020) of the UV photolysis of benzene ices, the authors observed a rapid desorption at ~140–150 K in vacuum conditions that could be related to the changes that we observe in the IR spectra of benzene ice at similar temperatures above 5×10^{-6} Torr in our experiment. Further studies in the future may help correlate potential temperature-sensitive phenomena to intrinsic ice properties of benzene and other compounds. Such studies would also prove useful for characterizing the inventory of organic deposits on planetary icy surfaces, as well as their scattering and surface texture properties. It is however beyond the scope of the study presented here.

4.3. Extent of the Polar Vortex Boundary

A recent state-of-the-art GCM study of Titan's atmosphere investigating the seasonal effects in the stratosphere (Vatant d'Ollone et al. 2018) has shown that the molecular enrichment of minor species in polar regions is seasonally driven by the global dynamics. The coupling between vapor condensation and latitudinal variations of species that can potentially form clouds therefore also depends on their vapor pressures. We have shown that our new experimental vapor pressure parameterization for benzene obtained at cold Titan-relevant temperatures impacts the gas vmr profiles (Figure 6) inferred from CIRS observational data, compared to previous analyses that used the F&S09 extrapolation (Vinatier et al. 2018). The C_6H_6 gas mixing ratio profiles retrieved from the 2013 May CIRS nadir observations above 83°S show strong differences compared to those at 78°S and at lower latitudes. Above 83°S, C_6H_6 becomes highly enriched, while below 78°S a sharp drop in benzene vmr is observed, indicating that the vortex boundary is most likely located between 83°S and 78°S. This finding is consistent with a recent analysis (Vinatier et al. 2020) of limb observations acquired two years later in March 2015, where a relatively sharp boundary of the southern polar vortex was observed around 80°S, as highlighted by the sharp southern polar molecular enrichment boundary inferred for several molecules. This polar enriched zone is explained by the strong zonal wind (polar vortex; see Figure 5 of Vinatier et al. 2020) isolating the enriched air transported from above by the subsiding branch of the global circulation from the air at mid- and low southern latitudes. Vinatier et al. (2020) showed that the polar vortex structure changed with time and most dramatically closer to the southern winter solstice. However, between 2013 and 2015, even though the southern polar stratosphere experienced a decrease in its temperature (Teanby et al. 2019; Vinatier et al. 2018), the polar vortex structure remained stable (Sharkey et al. 2021). During that two-year period, stratospheric temperatures were very cold (120–130 K) at locations where molecular mixing ratios were highly enriched, and similar trends were observed in the deep stratosphere.

Both nadir (in 2013 May) and limb (in 2015 March) results are consistent, and the sharp drop seen from 83°S to 78°S in the C_6H_6 volume gas mixing ratio (Figure 6) appears to further indicate that the vortex boundary is likely to be located between these two latitudes in 2013 May.

5. Conclusions

Ever since their first discovery in Titan's atmosphere, ice clouds and their contribution to Titan's global stratospheric dynamics, as well as thermal and chemical processes, have been investigated. Understanding the processes associated with the formation of ice clouds and their impact on the atmosphere, however, requires a robust knowledge of the fundamental microphysical parameters that control cloud nucleation and growth. Vapor pressures are one of these fundamental parameters as they are used in microphysics models to predict the temporal evolution of the cloud vertical structure and to constrain the expected cloud altitudes and particle sizes. Previously, the only Titan-like temperature (<160 K) C_6H_6 vapor pressures available in the literature to investigate the formation of benzene clouds in Titan's stratosphere were extrapolated from experimental data obtained at warmer temperatures (184–279 K, thus with a gap between 184 K and our region of interest <160 K).

We have experimentally measured, for the first time, the vapor pressures of C_6H_6 at temperatures relevant to Titan's stratospheric conditions in the south polar region (134–158 K). Our experimental measurements show that the C_6H_6 vapor pressures at cold temperatures are higher than the extrapolation most recently used for the analysis of Titan's observational data and in microphysics models. We have used a parameterization of our experimental low-temperature C_6H_6 vapor pressures to reanalyze CIRS observational data (from 2013 May) from 68°S to 87°S of the south polar cloud system that formed at unusually high altitudes (>250 km) after the northern spring equinox and retrieve the C_6H_6 gas vmr at each latitude and determine where condensation occurs. Using these new vapor pressures in the CIRS analysis results in benzene condensation occurring at lower altitudes in the stratosphere than previously thought. We have also used our experimental vapor pressures, along with the new mixing ratios from the CIRS reanalysis, in the CARMA model to simulate the formation of benzene ice clouds in Titan's stratosphere at 87°S. These simulations constrain C_6H_6 ice particle size distribution, gas vmr's, gas relative humidity, and cloud altitudes down to lower altitudes that are not accessible with CIRS observations. The simulations predict greater C_6H_6 gas mixing ratios below the condensation level than with previous vapor pressure extrapolations, resulting in more C_6H_6 being available per cloud particle to condense at stratospheric levels (<250 km) and hence a growth in size distribution, in particular between 125 km and 50 km. At 87°S, as observed with the CIRS data reanalysis, the CARMA model predicts benzene condensation occurring deeper in the stratosphere. From the reanalysis of Cassini CIRS observations at latitudes spanning from 68°S to 87°S, we also inferred that the vortex polar boundary in 2013 resided between 78°S and 83°S. From 83°S to 87°S, the cloud top would be located between 246 and 256 km, and from 68°S to 78°S, it would be located between 90 and 110 km.

This research was supported by the CDAP Program of NASA SMD. The authors acknowledge outstanding technical support from Emmett Quigley, as well as helpful discussions with Dr. Bernard Schmitt on phase changes and the crystallinity of low-temperature astrophysically relevant ices.

ORCID iDs

David Dubois https://orcid.org/0000-0003-2769-2089
Farid Salama https://orcid.org/0000-0002-6064-4401
Sandrine Vinatier https://orcid.org/0000-0001-5541-2502
Ella Sciamma-O'Brien https://orcid.org/0000-0002-1883-552X

References

Anderson, C. M., & Samuelson, R. E. 2011, Icar, 212, 762
Anderson, C. M., Samuelson, R. E., Achterberg, R. K., Barnes, J. W., & Flasar, F. M. 2014, Icar, 243, 129
Anderson, C. M., Samuelson, R. E., & Nna-Mvondo, D. 2018, SSRv, 214, 125
Anderson, C. M., Samuelson, R. E., Yung, Y. L., & McLain, J. L. 2016, GeoRL, 43, 3088
Barth, E. L. 2017, P&SS, 137, 20
Barth, E. L., & Toon, O. B. 2003, Icar, 162, 94
Bernhardsson, A., Forsberg, N., Malmqvist, P. Å., Roos, B. O., & Serrano-Andrés, L. 2000, JChPh, 112, 2798
Borucki, W. J., & Tripathi, S. 1987, JGRE, 112, 604
Borucki, W. J., Whitten, R. C., Bakes, E. L. O., Barth, E., & Tripathi, S. 2006, Icar, 181, 527
Chandrasekaran, V., Biennier, L., Arunan, E., Talbi, D., & Georges, R. 2011, JPCA, 115, 11263
Coustenis, A., Jennings, D. E., Achterberg, R. K., et al. 2016, Icar, 270, 409
Coustenis, A., Schmitt, B., Khanna, R. K., & Trotta, F. 1999, P&SS, 47, 1305
Curtis, D. B., Rajaram, B., Toon, O. B., & Tolbert, M. A. 2005, ApOpt, 44, 4102
Dawes, A., Pascual, N., Hoffmann, S. V., Jones, N. C., & Mason, N. J. 2017, PCCP, 19, 27544
Dawes, A., Pascual, N., Mason, N. J., Gärtner, S., Hoffmann, S. V., & Jones, N. C. 2018, PCCP, 20, 15273

De Kok, R. J., Teanby, N. A., Maltagliati, L., Irwin, P. G. J., & Vinatier, S. 2014, Natur, 514, 65
De Kruif, C. G., & Van Ginkel, C. H. D. 1977, The Journal of Chemical Thermodynamics, 9, 725
Deitz, V. R. 1933, J. Am. Chem. Soc., 55, 472
Dubois, D., Sciamma-O'Brien, E., Iraci, L. T., et al. 2019, in IAU Symp. 350, Laboratory Astrophysics: From Observations to Interpretation, ed. F. Salama & H. Linnartz (Cambridge: Cambridge Univ. Press), 189
Engdahl, A., & Nelander, B. 1985, J. Phys. Chem., 89, 2860
Fulchignoni, M., Ferri, F., & Angrilli, F. 2005, Natu, 438, 785
Fray, N., & Schmitt, B. 2009, P&SS, 57, 2053
Grundy, W. M., Schmitt, B., & Quirico, E. 1993, Icar, 105, 254
Grundy, W. M., Schmitt, B., & Quirico, E. 2002, Icar, 155, 486
Gudipati, M. S., Jacovi, R., Couturier-Tamburelli, I., Lignell, A., & Allen, M. 2013, NatCo, 4, 1648
Ha, H., Morrison, J. A., & Richards, E. L. 1976, J. Chem. Soc., 72, 1051
Iraci, L. T., Phebus, B. D., Stone, B. M., & Colaprete, A. 2010, Icar, 210, 985
Jackowski, A. W. 1974, The Journal of Chemical Thermodynamics, 6, 49
Jasper, J. J. 1972, JPCRD, 1, 841
Jennings, D. E., Achterberg, R. K., Cottini, V., et al. 2015, ApJL, 804, 1
Kearley, G. J., Johnson, M. R., & Tomkinson, J. 2006, JChPh, 124, 044514
Khanna, R. K. 2005a, Icar, 178, 165
Khanna, R. K. 2005b, Icar, 177, 116
Kim, S. J., Geballe, T. R., Noll, K. S., & Courtin, R. 2005, Icar, 173, 522
Lebonnois, S., Burgalat, J., Rannou, P., & Charnay, B. 2012, Icar, 218, 707
Le Mouélic, S., Cornet, T., Rodriguez, S., et al. 2018, Icar, 319, 121
Lide, D. R. 2006, CRC Handbook of Chemistry and Physics (87th edn.; Boca Raton, FL: CRC Press), 2388
Lora, J. M., Lunine, J. I., & Russell, J. L. 2015, Icar, 250, 516
Mathé, C., Vinatier, S., Bézard, B., et al. 2020, Icar, 344, 113547
Milazzo, G. 1956, Ann. Chim., 1105, (Roma 46)
Mouzay, J., Couturier-Tamburelli, I., Piétri, N., & Chiavassa, T. 2020, JGRE, 126, e06566
Nelander, B. 1985, JChPh, 82, 5340
Newman, C. E., Richardson, M. I., Lian, Y., & Lee, C. 2016, Icar, 267, 106
Niemann, H. B., Atreya, S. K., Demick, J. E., et al. 2010, JGRE, 115, E12006
Pruppacher, H. R., & Klett, J. D. 1997, Microphysics of Clouds and Precipitation (1st ed.; Berlin: Springer)
Quirico, E. 1995, Thèse de l'Université Joseph Fourier (Grenoble), https://www.theses.fr/1995GRE10237
Quirico, Eric., Schmitt, B., Bini, R., & Salvi, P. R. 1996, P&SS, 44, 973
Rannou, P., Curtis, D., & Tolbert, M. A. 2019, A&A, 631, A151
Růžička, K., Fulem, M., & Červinka, C. 2014, Journal of Chemical Thermodynamics, 68, 40
Sagan, C., & Thompson, W. 1984, Icar, 59, 133
Samuelson, R. E., Mayo, L. A., Knuckles3, M. A., & Khanna4, R. J. 1997, P&SS, 45, 941
Sharkey, J., Teanby, N. A., Sylvestre, M., et al. 2021, Icar, 354, 114030
Teanby, N., Bézard, B., Vinatier, S., et al. 2017, NatCo, 8, 1586
Teanby, N., Irwin, P. G. J., Nixon, C. A., et al. 2012, Natur, 491, 732
Teanby, N. A., Sylvestre, M., Sharkey, J., et al. 2019, GeoRL, 46, 3079
Vatant d'Ollone, J., Fletcher, L. N., Guerlet, S., et al. 2020, 14th Europlanet Science Congress 2020, EPSC2020-292
Vatant d'Ollone, J., Lebonnois, S., & Burgalat, J. 2018, EPSC Abstracts, 12, EPSC2018-1034
Vinatier, S., Bézard, B., Lebonnois, S., et al. 2015, Icar, 250, 95
Vinatier, S., Mathé, C., Bézard, B., et al. 2020, A&A, 641, A116
Vinatier, S., Schmitt, B., Bézard, B., et al. 2018, Icar, 310, 89
Wilson, E. B., Decius, J. C., & Cross, P. C. 1955, Molecular Vibrations (New York: McGraw-Hill)